

Structural transitions of epitaxial ceria films on Si(111)

Cite this: *Phys. Chem. Chem. Phys.*, 2013, **15**, 18589
H. Wilkens,^a O. Schuckmann,^a R. Oelke,^a S. Gevers,^a M. Reichling,^a A. Schaefer,^b
M. Bäumer,^b M. H. Zoellner,^c G. Niu,^c T. Schroeder^{cd} and J. Wollschläger^{*a}

The structural changes of a (111) oriented CeO₂ film grown on a Si(111) substrate covered with a hex-Pr₂O₃(0001) interface layer due to post deposition annealing are investigated. X-ray photoelectron spectroscopy measurements revealing the near surface stoichiometry show that the film reduces continuously upon extended heat treatment. The film is not homogeneously reduced since several coexisting crystalline ceria phases are stabilized due to subsequent annealing at different temperatures as revealed by high resolution low energy electron diffraction and X-ray diffraction. The electron diffraction measurements show that after annealing at 660 °C the *r*-phase (Ce₇O₁₂) is formed at the surface which exhibits a ($\sqrt{7} \times \sqrt{7}$)R19.1° structure. Furthermore, a ($\sqrt{27} \times \sqrt{27}$)R30° surface structure with a stoichiometry close to Ce₂O₃ is stabilized after annealing at 860 °C which cannot be attributed to any bulk phase of ceria stable at room temperature. In addition, it is shown that the fully reduced ceria (Ce₂O₃) film exhibits a bixbyite structure. Polycrystalline silicate (CeSi_xO_y) and crystalline silicide (CeSi_{1.67}) are formed at 850 °C and detected at the surface after annealing above 900 °C.

Received 27th June 2013,
Accepted 4th September 2013

DOI: 10.1039/c3cp52688g

www.rsc.org/pccp

1 Introduction

Ceria plays a key role in the field of catalysis. For instance, ceria is used in several reactions¹ like the three-way automotive exhaust catalysis² or the generation of hydrogen.³ The catalytic activity is strongly influenced by oxygen vacancies especially at the surface. Hence, it is necessary to control the density and distribution of oxygen vacancies to build ceria based catalysts with tailored reactivity and selectivity. For obtaining a deep insight into the complex chemical reactions a single crystalline film with (111) orientation can be used as a ceria model catalyst where the atomic structure of surface and sub-surface oxygen vacancies is well known.⁴ Using a two dimensional film instead of a polycrystalline three dimensional structure facilitates the use of a variety of surface science techniques^{5–7} since these films exhibit a well-defined crystalline structure⁸ and surface morphology.⁹

Here, silicon with (111) orientation is a well-suited substrate since CeO₂ exhibits a small lattice mismatch (−0.35%) with respect to Si(111).^{10–12} Furthermore, ultrathin ceria films on Si substrates are very attractive since ceria is a well-known insulating buffer layer for functional oxide integration in the field of micro- and nanoelectronics due to its high dielectric constant (≈ 26).

In addition, recent studies reveal the existence of room temperature ferromagnetism (RTFM) in doped and reduced ceria giving the opportunity for combining future spintronic devices with the existing silicon based technology.^{13–18} Oxygen vacancies have a strong influence on the magnetic properties in reduced ceria. However, the origin of this magnetism has not unambiguously been resolved up to now. The controlled generation of oxygen vacancies with long range order, as presented in this study, can be used to examine the role of oxygen vacancies in future studies elucidating the magnetic properties in more detail.

For bulk materials, the cerium–oxygen phase diagram exhibits several intermediate phases^{19–21} between the highest (CeO₂) and lowest oxidation states (Ce₂O₃). It is still a challenge to stabilize intermediate phases for thin films with high structural control. Recently, we have demonstrated that it is possible to stabilize the surface of the ceria *r*-phase (Ce₇O₁₂) on a hex-Pr₂O₃(0001)–Si(111) system due to the reduction of a CeO₂(111) film.²² However, it is not yet clear whether the entire film is reduced to the Ce₇O₁₂ structure and whether it is possible to stabilize other intermediate phases. Therefore, we conduct a detailed study of the structural changes of a 250 nm CeO₂(111) film grown on a hex-Pr₂O₃(0001)–Si(111) system⁸ addressing, both, the surface and the bulk stoichiometry and crystal structure for different post deposition annealing (PDA) temperatures.⁹ The oxidation state of the surface is determined *via* X-ray photoelectron spectroscopy (XPS) while experiments with high resolution low energy electron diffraction combined with spot profile analysis (SPA-LEED) are performed to determine the changes in the atomic structure at the surface. In addition,

^a Fachbereich Physik, Universität Osnabrück, Barbarastr. 7, 49076 Osnabrück, Germany. E-mail: joachim.wollschlaeger@uos.de

^b Institute of Applied and Physical Chemistry, University of Bremen, Leobener Str. NW2, 28359 Bremen, Germany

^c IHP, Im Technologiepark 25, 15236 Frankfurt(Oder), Germany

^d BTU Cottbus, Institute of Physics, Konrad-Zuse-Str. 1, 03046 Cottbus, Germany

transitions of the crystal structure throughout the film are investigated using synchrotron based *in situ* X-ray diffraction (XRD) measurements.

2 Experiment

Ceria films are grown *via* molecular beam epitaxy (MBE) on boron doped 4" Si(111) wafers ($\sigma = 5\text{--}15 \text{ } \Omega \text{ cm}$) which are cleaned and hydrogen terminated according to the recipe described in ref. 23. After loading the wafer into an ultrahigh vacuum (UHV) chamber (base pressure 10^{-10} mbar) and annealing at 700 °C for 5 min, the Si(111)(7×7) surface reconstruction is obtained. An ultrathin hex-Pr₂O₃(0001) buffer layer is grown at a substrate temperature of 625 °C and a deposition rate of 3 nm min⁻¹.²⁴ The growth is monitored *via* reflection high-energy electron diffraction (RHEED) and the deposition is stopped after complete coverage of the substrate is reached (thickness ≈ 3 nm). Afterwards, a cub-CeO₂(111) film (thickness ≈ 250 nm) is deposited using the same substrate temperature and deposition rate. The CeO₂(111) film exhibits the fluorite crystal structure and a high crystalline quality as confirmed by *ex situ* XRD (data not shown).

The surface characterization is performed in two different UHV chambers (base pressure 10^{-10} mbar for both). The first chamber is equipped with a SPA-LEED system and the samples are annealed *via* resistive heating of the Si substrates. XPS measurements using Al K _{α} radiation (1486.6 eV) are performed in a second chamber where the surface structure is controlled using a conventional LEED while the samples are annealed *via* filament heating. For both experimental setups, samples are successively annealed for 30 min and the temperature is controlled using an infrared (IR) pyrometer. After each PDA step the samples are cooled to room temperature (RT) to perform the measurements. When resistive heating is used, samples cool to room temperature almost immediately (cooling rate $\approx 500 \text{ } ^\circ\text{C min}^{-1}$). If annealed *via* filament the sample cooling takes several hours (cooling rate $\approx 5 \text{ } ^\circ\text{C min}^{-1}$) due to the large heat capacity of the sample holder.

The exposure of praseodymia films to an oxygen plasma has proven to be a superior method to gain high quality praseodymium dioxide (PrO₂) surfaces²⁶ and here we adopt this concept to ceria films. Hence, prior to the SPA-LEED and XPS experiments, samples are transferred to an *in situ* plasma chamber (base pressure 10^{-7} mbar) and exposed to an oxygen microwave plasma (2.45 GHz) for 15 min to clean the surface and to reduce the number of oxygen vacancies at the surface. The plasma parameters are 80 sccm gas flow, 0.26 mbar oxygen pressure and 360 W power. Due to this treatment, the overall intensity of the XP spectra increases and the previously present weak carbon 1s signal ($E_B = 284$ eV) due to carbon contamination vanishes (data not shown). Furthermore, in the electron diffraction measurements the diffuse background intensity is drastically reduced and strong charging effects appear indicating the high quality of the film. Hence, oxygen plasma treatment is a suitable method for cleaning and improving the crystalline quality of CeO₂ films.

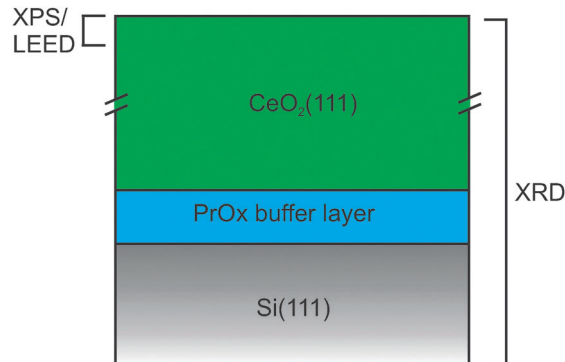


Fig. 1 Schematic drawing of the investigated system. XPS and LEED are used to probe the near surface region while changes of the entire structure are studied by XRD.

For the structural characterization of the entire film, untreated samples are investigated using *in situ* X-ray diffraction (XRD) measurements carried out in a modified version of the high vacuum (HV) reaction chamber (base pressure 10^{-8} mbar) presented in ref. 25. The heating stage has been modified to enable resistive heating and an IR pyrometer was added for temperature control. The HV reaction chamber was mounted on a six-circle diffractometer at beamline W1 at DESY (Hamburg, Germany) facilitating diffraction studies with a photon energy of 10.5 keV. All measurements were performed at RT.

A schematic drawing of the investigated system is shown in Fig. 1.

3 Results

3.1 XPS

We determine the stoichiometry of the ceria surface after successive annealing cycles at different temperatures *via* XPS. The different oxidation states of ceria have extensively been studied by XPS in the past.^{27–30} Factor analysis studies have shown that the reduction process of ceria can be described by the two components of Ce³⁺ and Ce⁴⁺.^{31–33} Therefore, the oxidation state of the surface can be determined with high accuracy using a superposition of Ce 3d spectra of both Ce₂O₃ and CeO₂ since these spectra solely containing Ce³⁺ and Ce⁴⁺ cations, respectively. The plasma treated sample is used for the CeO₂ reference spectrum while the Ce₂O₃ reference spectrum is obtained after annealing the sample at 890 °C with respective results shown in Fig. 2.

In the latter case, we assume a completely reduced film since LEED measurements show the (4×4) structure related to the expected bixbyite cub-Ce₂O₃ phase (*cf.* Fig. 6) while silicide is formed at higher temperatures as further discussed in the following. Furthermore, these reference spectra are in very good agreement with previously calculated spectra by Kotani and Ogasawara.³⁵

Fig. 2 shows a series of Ce 3d XP spectra with the corresponding fits after successive annealing cycles at different

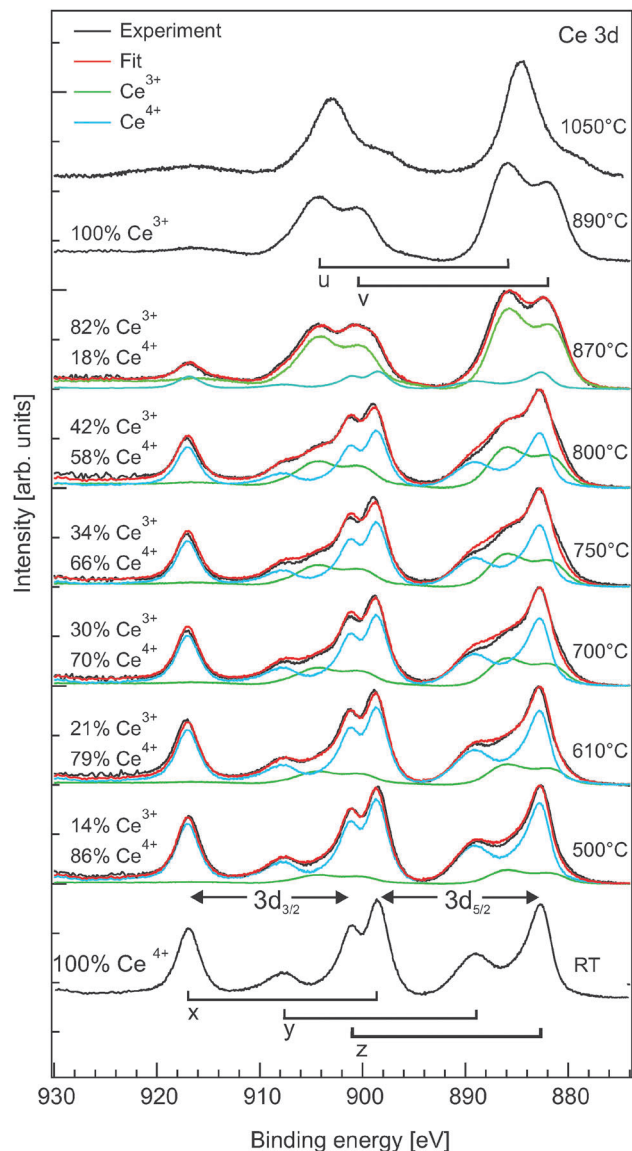


Fig. 2 XP spectra of the Ce 3d region. The area underneath the peaks is normalized to unity after a Shirley background is subtracted. The CeO₂ spectrum measured on the plasma treated sample consists of three peaks (x, y, z) for each of the 3d_{5/2} and 3d_{3/2} components. All cations have the Ce⁴⁺ valence state. The near surface region is fully reduced to Ce₂O₃ after annealing at 890 °C where all cations have the Ce³⁺ valence state. The spectrum consist of two peaks (u, v) in each of the 3d_{5/2} and 3d_{3/2} components. The determination of the Ce³⁺/Ce⁴⁺ ratio of the intermediate states was done by fitting the spectra with a weighted linear combination of the CeO₂ and Ce₂O₃ spectra. After annealing at 1050 °C the peaks u and v shift ≈ 1.2 eV and ≈ 2.8 eV to lower binding energies due to silicide or silicate formation.

temperatures. Prior to the fitting, a Shirley background is subtracted and the area underneath the peaks is normalized to unity. The fits are in very good agreement with the measured spectra allowing a determination of the Ce³⁺/Ce⁴⁺ ratio with an accuracy of 3%. The spin-orbit splitting in all Ce 3d spectra attributed to ceria is ≈ 18 eV.

In the following, the origin and nomenclature of the peaks appearing in the 3d spectra presented in Fig. 2 are briefly

introduced according to Kotani's theory. Valence band holes and core holes are denoted as \bar{v} and \bar{c} , respectively. The ground state of CeO₂ consists of the hybridization of the 4f⁰ and 4f¹ \bar{v} configurations according to Kotani's theory which leads to three final states (x, y, z) in each of the 3d_{5/2} and 3d_{3/2} components. The peaks labeled with x and y correspond to the bonding and antibonding final states of the strongly hybridized 4f¹ $\bar{v}\bar{c}$ and 4f² $\bar{v}^2\bar{c}$ configurations while the peak labeled with z corresponds to the pure 4f⁰ \bar{c} final state. On the contrary, the ground state of Ce₂O₃ exhibits only the pure 4f¹ configuration, which leads to two final states in each 3d_{5/2} and 3d_{3/2} component. The peaks labeled with u and v in the Ce 3d spectrum of Ce₂O₃ correspond to the bonding and the antibonding final states of the hybridized 4f¹ \bar{c} and 4f² $\bar{v}\bar{c}$ configurations, respectively.

Fig. 3 presents the amount of Ce³⁺ cations at the near surface region (inelastic mean free path $\lambda \approx 10$ Å in CeO₂)³⁴ of the film after the different annealing steps. The surface reduces continuously as shown by the increasing amount of Ce³⁺ cations with increasing PDA temperature. Until a PDA temperature of ≈ 800 °C is reached, the Ce³⁺ concentration shows only a slight increase. Thereafter, the oxygen release at the surface is drastically increased. After PDA treatments at temperatures higher than 890 °C the peaks labeled with u and v shift ≈ 1.2 eV and ≈ 2.8 eV to lower binding energies, respectively. In addition, the intensity of the peak labeled with v is strongly reduced. This 3d spectrum appears like a metallic cerium spectrum^{36,37} superimposed with a weak Ce₂O₃ spectrum.³⁵

These results are supported by Ce 4d spectra presented in Fig. 4 that show the transition from a CeO₂ to a Ce₂O₃ spectrum with increasing PDA temperature. The measurements of the untreated and 890 °C annealed sample are in good agreement with the spectra of 4d CeO₂ and Ce₂O₃ calculated by Kotani and Ogasawara,³⁵ respectively. The 4d spectra are only slightly separated into 4d_{5/2} and 4d_{3/2} components since the spin orbit splitting is much weaker than for the 3d spectra. Furthermore, this weak splitting cannot be resolved due to the strong

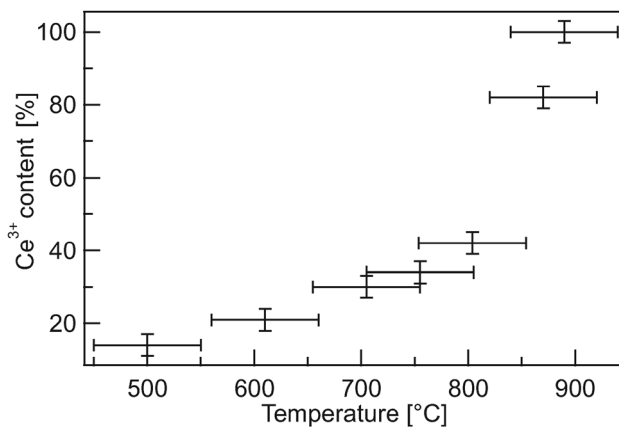


Fig. 3 Plot of the Ce³⁺ concentration as determined by the analysis of the Ce 3d spectra against the annealing temperature. The near surface region is continuously reduced with increasing temperature. After annealing at temperatures above 800 °C, the Ce³⁺ concentration increases drastically.

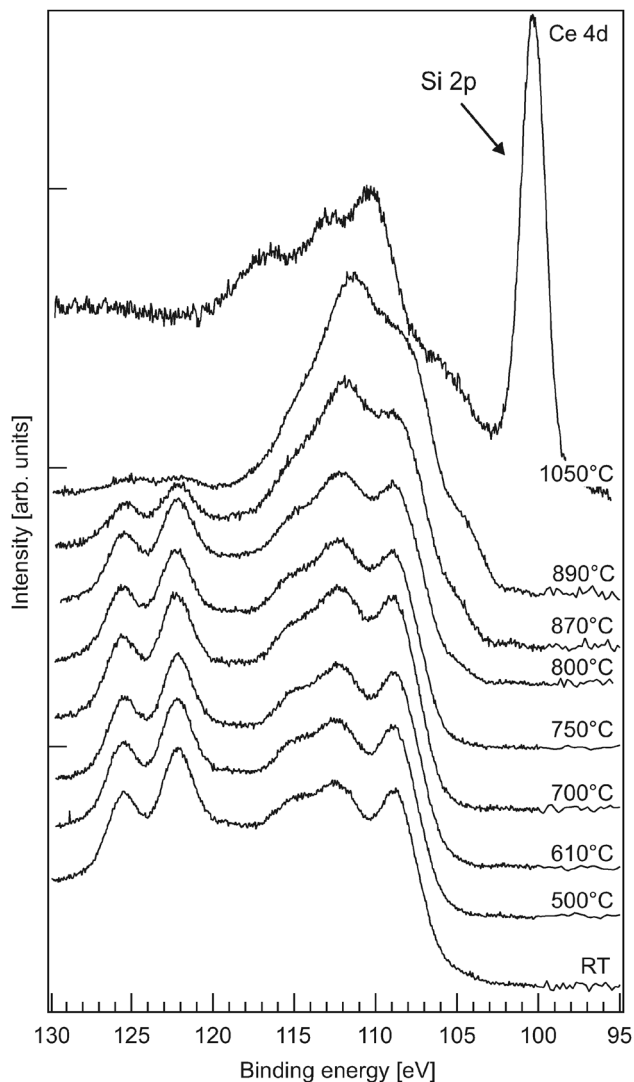


Fig. 4 XP spectra of the Ce 4d region normalized to the Ce 3d signal. After annealing at 1050 °C a strong Si 2p peak ($E_B = 100.3$ eV) appears.

overlapping multiplet coupling of the 4d and 4f states. Similar to the Ce 3d spectra, the intermediate spectra consist of a superposition of the CeO_2 and Ce_2O_3 spectra. The spectral weight of the characteristic features attributed to the CeO_2 4d spectrum, *e.g.* the components located at $E_B = 125.5$ eV and $E_B = 122.2$ eV, decreases with increasing PDA temperature while the spectral weight of the characteristic features attributed to the Ce_3O_2 4d spectrum increases. Furthermore, a strong Si 2p signal ($E_B = 100.3$ eV) close to the Ce 4d signals appears after annealing at 1050 °C indicating film decomposition by the diffusion of silicon to the surface.

Fig. 5 shows the O 1s spectra after subsequent annealing at different temperatures. For each measurement the spectrum is normalized to the area of the Ce 3d peaks. The O 1s peak attributed to ceria is located at $E_B = 530.2$ eV and exhibits a very weak shoulder at $E_B \approx 532$ eV. The origin of this shoulder is not clear. Some authors assign this shoulder to isolated oxygen vacancies in the ceria lattice²⁷ while others attribute it to surface impurities like hydroxyl groups.^{28,38,39}

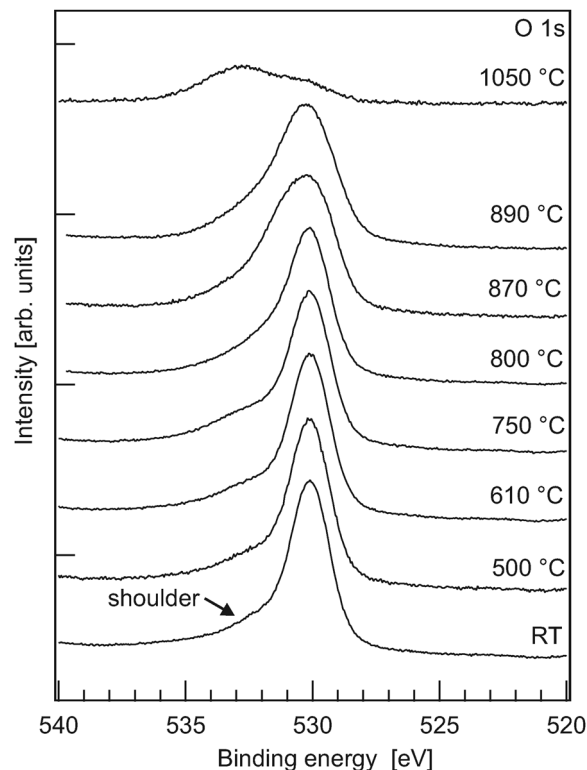


Fig. 5 XP spectra of the O 1s peak ($E_B = 530.2$ eV) exhibiting a weak shoulder at $E_B \approx 532$ eV. The spectra are normalized to the Ce 3d signal. The FWHM of the O 1s peak increases after annealing above 800 °C. The intensity of the O 1s peak is drastically reduced after annealing at 1050 °C and the shoulder shifts to higher binding energies indicating Si–O bonds.

The intensity of the O 1s signal attributed to ceria decreases with higher PDA temperatures which is consistent with the increase of the Ce^{3+} signal in the Ce 3d spectra due to oxygen loss during film reduction. However, the weak shoulder is almost unchanged during the PDA treatment. Taking into account our LEED results, which prove that ordered oxygen vacancies emerge at the surface (*cf.* Section 3.2), we conclude that surface contamination is the origin of the shoulder and not oxygen vacancies. On the contrary, the full width at half-maximum (FWHM) of the O 1s peak increases from ≈ 1.6 eV to ≈ 2.5 eV after annealing above 800 °C. A possible explanation for this effect is a roughening of the surface due to oxygen vacancies caused by the massive release of oxygen in this temperature region (*cf.* Fig. 3). After annealing above 900 °C the intensity of the O 1s peak attributed to ceria is drastically decreased which is in good agreement with the Ce 3d spectra and points to the formation of silicide or silicate instead of oxide. Thus, large areas of the surface are transformed into silicide or silicate and only a small amount of ceria is left at the surface.

3.2 SPA-LEED

Structural changes at the surface are investigated using electron diffraction measurements. Fig. 6 shows diffraction patterns of the appearing structures. A hexagonal pattern with a

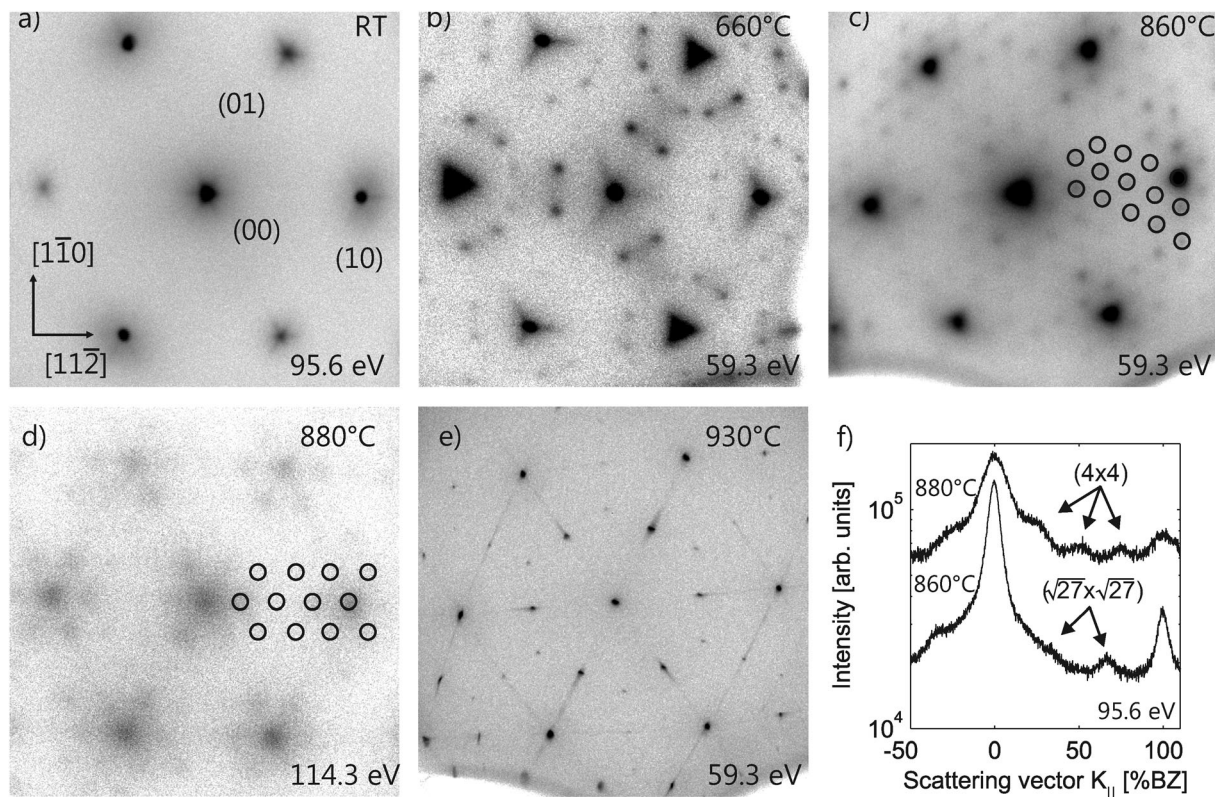


Fig. 6 Two dimensional SPA-LEED pattern of the appearing structures close to Bragg conditions (in-phase) of $\text{CeO}_2(111)$. (a) The (1×1) structure of the sample stays unchanged at low and moderate temperatures. (b) At a PDA temperature of 660°C a $(\sqrt{7} \times \sqrt{7})\text{R}19.1^\circ$ superstructure attributed to the ι -phase (Ce_7O_{12}) appears. (c) In the narrow temperature region of $850\text{--}870^\circ\text{C}$ a $(\sqrt{27} \times \sqrt{27})\text{R}30^\circ$ structure forms. (d) A weak (4×4) structure assigned to the bixbyite phase of Ce_2O_3 appears at PDA temperatures of $880\text{--}890^\circ\text{C}$. (e) After annealing above 900°C , a sharp (2×1) pattern superimposed with a $(\sqrt{3} \times \sqrt{3})\text{R}30^\circ$ structure appears which can be assigned to cerium silicide. (f) Cross section along the $[11\bar{2}]$ direction. The $(\sqrt{27} \times \sqrt{27})\text{R}30^\circ$ and the (4×4) structures show two and three peaks between the fundamental diffraction spots, respectively.

threefold symmetry of the intensity of the first order diffraction spots is visible for the plasma treated sample (*cf.* Fig. 6(a)). This threefold intensity distribution is caused on the ABC layer stacking sequence along the $\langle 111 \rangle$ directions of the cubic fluorite structure of CeO_2 . Furthermore, at several electron energies, the shape of the main spots becomes triangular indicating the formation of tetrahedral pyramids on the ceria surface (see also ref. 48).

After annealing at 660°C , a $(\sqrt{7} \times \sqrt{7})\text{R}19.1^\circ$ superstructure with two mirror domains appears (*cf.* Fig. 6(b)). This superstructure can be attributed to the surface structure of the ι -phase (Ce_7O_{12}) of ceria which is based on ordered oxygen vacancies along the $\langle 111 \rangle$ directions in the bulk fluorite CeO_2 structure.²² While the intensity of the fundamental diffraction spots stays almost constant, the intensity of the $(\sqrt{7} \times \sqrt{7})\text{R}19.1^\circ$ superstructure spots decreases with higher annealing temperatures.

Applying PDA temperatures in the region of $850\text{--}880^\circ\text{C}$ leads to the formation of a $(\sqrt{27} \times \sqrt{27})\text{R}30^\circ$ structure (*cf.* Fig. 6(c)). Note, that there is no sharp transition from the $(\sqrt{7} \times \sqrt{7})\text{R}19.1^\circ$ to the $(\sqrt{27} \times \sqrt{27})\text{R}30^\circ$ structure. After annealing at 850°C a superposition of these two patterns is measured but the intensity of the $(\sqrt{7} \times \sqrt{7})\text{R}19.1^\circ$ diffraction peaks is very weak. Thus, both

phases coexist for these treatments. Taking into account the XPS results, the $(\sqrt{27} \times \sqrt{27})\text{R}30^\circ$ structure corresponds to a stoichiometry close to Ce_2O_3 with excess oxygen.

After PDA at 880°C , a weak (4×4) pattern appears (*cf.* Fig. 6(d)) that can be attributed to the bixbyite structure of cub- Ce_2O_3 similar to cub- $\text{Pr}_2\text{O}_3(111)$ grown on $\text{Si}(111)$.^{40,41} Fig. 6(f) compares cross sections of the diffraction patterns from the (4×4) bixbyite structure (upper curve) and the $(\sqrt{27} \times \sqrt{27})\text{R}30^\circ$ structure. These line scans are normalized to the (surface) Brillouin-zone size (BZ) of $\text{CeO}_2(111)$ (lateral row distance $a_{\text{CeO}_2} = 3.314 \text{ \AA}$).

After annealing above 900°C , a sharp (2×1) pattern with weak streaks between the fundamental diffraction spots appears (*cf.* Fig. 6(e)). This pattern is superimposed with a $(\sqrt{3} \times \sqrt{3})\text{R}30^\circ$ pattern and has been assigned to different surface phases of cerium silicide.^{42,43} In addition, very weak polycrystalline rings become visible at several electron energies (data not shown). These findings are in good agreement with the XPS results since a strong Si 2p signal ($E_B = 100.3 \text{ eV}$) appears when annealing at temperatures above 900°C (*cf.* Fig. 4) indicating the segregation of Si to the surface.

A detailed spot profile analysis is performed after each annealing cycle to get deeper insight of the near surface structure and

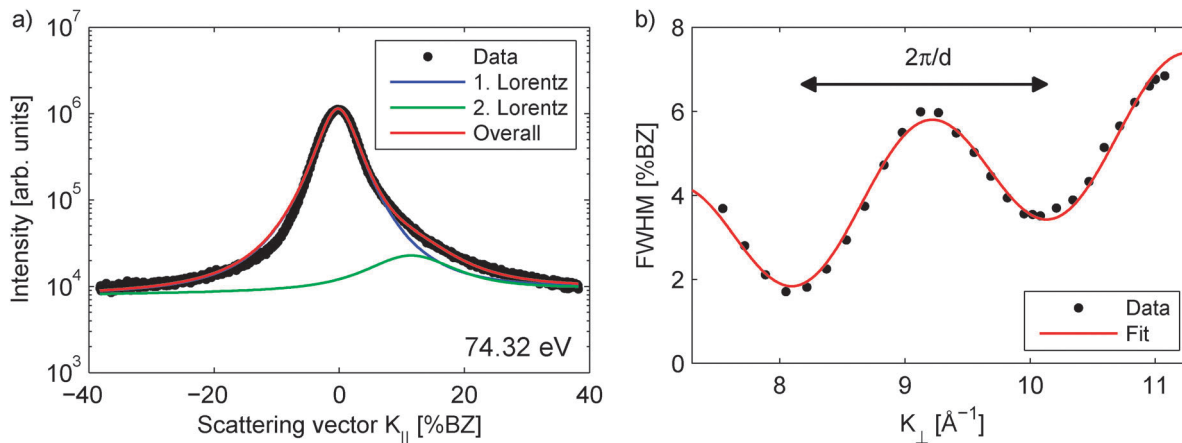


Fig. 7 (a) Cross section in the SPA-LEED pattern along the $[11\bar{2}]$ direction after annealing at $500\text{ }^{\circ}\text{C}$ for 30 min. The central peak (blue) and the shoulder (green) are fitted with Lorentzian functions. (b) FWHM of the central peak plotted against K_{\perp} after annealing at $500\text{ }^{\circ}\text{C}$ for 30 min. The fit according to eqn (1) is in good agreement with the experimental data.

surface morphology. In the following, K_{\parallel} and K_{\perp} denote the lateral and vertical components of the scattering vector with respect to the sample surface. Cross-sections (line scans) are measured through the (00)-spot along the $[11\bar{2}]$ direction. The data were fitted with two Lorentzian functions, one sharp and intense component for the central diffraction spot and the other for the appearing broad and weak shoulders due to the triangular reflex shape (cf. Fig. 7(a)).

The first function has its center at $K_{\parallel} = 0$ (central peak), while the lateral position of the shoulder changes with K_{\perp} . This behavior of the shoulder is caused by facets at the film surface.^{44,45} The FWHM of the central peak oscillates with K_{\perp} (cf. Fig. 7(b)) indicating that flat terraces are separated by atomic steps. These oscillations can be fitted by the function

$$\text{FWHM}(K_{\perp}) = 100\% \text{BZ} \frac{a_{\text{CeO}_2} \sqrt{2^{2/3} - 1}}{\pi} \left(\frac{1 - \cos(dK_{\perp})}{\langle \Gamma \rangle} \right) \quad (1)$$

according to the model presented in ref. 46 and 47. Here, d denotes the step height and $\langle \Gamma \rangle$ the mean terrace width. Compared to ref. 46 the prefactor $\sqrt{2^{2/3} - 1}$ is needed to describe the isotropic exponentially decaying 2D correlation.

The spot profile analysis for PDA temperatures up to $660\text{ }^{\circ}\text{C}$ yields the same results within experimental error (independent of the annealing temperature). An average step height of $d = (3.09 \pm 0.05)\text{ \AA}$ close to the bulk value of the $\text{CeO}_2(111)$ crystal plane spacing ($c_{\text{CeO}_2} = 3.124\text{ \AA}$) is determined in accordance with recent studies by non-contact atomic force microscopy.⁴⁸ Furthermore, the average terrace width ($\langle \Gamma \rangle = (6.0 \pm 0.5)\text{ nm}$) does not change significantly in this temperature region. These results are in good agreement with the XRD results described in the following section which also show no change of the bulk structure for low annealing temperatures.

For PDA temperatures above $660\text{ }^{\circ}\text{C}$, the oscillating part of the FWHM curves is strongly diminished indicating the formation of large terraces beyond the resolution of our instrument. The smoothing of the ceria film surface, however, has

also been observed in a NC-AFM study on similar films⁴⁸ with an overall morphology closely resembling that of a (111)-surface of bulk ceria.^{9,49}

3.3 XRD results

Reciprocal space mappings of *in situ* XRD measurements, as well as, (00L) crystal truncation rods (CTRs) after annealing at different temperatures are presented in Fig. 8 and 9, respectively. The measurements after each annealing step are performed at RT, too. In the following, the subscripts S and B denote surface and bulk coordinates, respectively. The component of the scattering vector K_{\perp} normal to the surface is scaled to reciprocal lattice units (r.l.u.) of the silicon substrate *via* $L = 2\pi K_{\perp}/c_{\text{Si}}$ where $c_{\text{Si}} = 3.136\text{ \AA}$ denotes the vertical layer spacing of $\text{Si}(111)$. Thus, the peaks denoted by $(00L)_S$ correspond to the $(LLL)_B$ bulk Bragg peaks.

Fig. 8 shows reciprocal space mappings of the specular $(00L)$ -rod close to the $\text{Si}(111)_B$ Bragg peak which is equivalent to $\text{Si}(001)_S$. For the as grown samples, a broad oxide Bragg peak next to the sharp silicon peak is visible at slightly larger L values than Si. This peak can be attributed to CeO_2 . After annealing at elevated temperatures, further Bragg peaks appear at lower L values due to intermediate ceria phases with reduced oxygen content or cerium silicide. Starting at $850\text{ }^{\circ}\text{C}$ elongated features indicating a polycrystalline structure appear at $L = 0.889, 1.089, 1.099$ and 1.128 in the reciprocal space mappings. These structures can not be unambiguously assigned to any cerium silicate (CeSi_xO_y) or silicide (CeSi_x) phase.

CTR scans at $K_{\parallel} = 0\text{ \AA}^{-1}$ of the $(00L)$ CTR are performed for a detailed analysis of the appearing Bragg peaks with results shown in Fig. 9. The untreated sample shows the $\text{CeO}_2(111)_B$ Bragg peak at $L = 1.005$ corresponding to a vertical layer distance of $c_{\text{CeO}_2} = 3.120\text{ \AA}$ (bulk $c_{\text{CeO}_2} = 3.124\text{ \AA}$) next to the narrow $\text{Si}(111)_B$ peak ($L = 1$). Furthermore, fringes of the praseodymia buffer layer are well discernible due to its very homogeneous thickness. These fringes do not change for all PDA treatments at temperatures below or equivalent to a

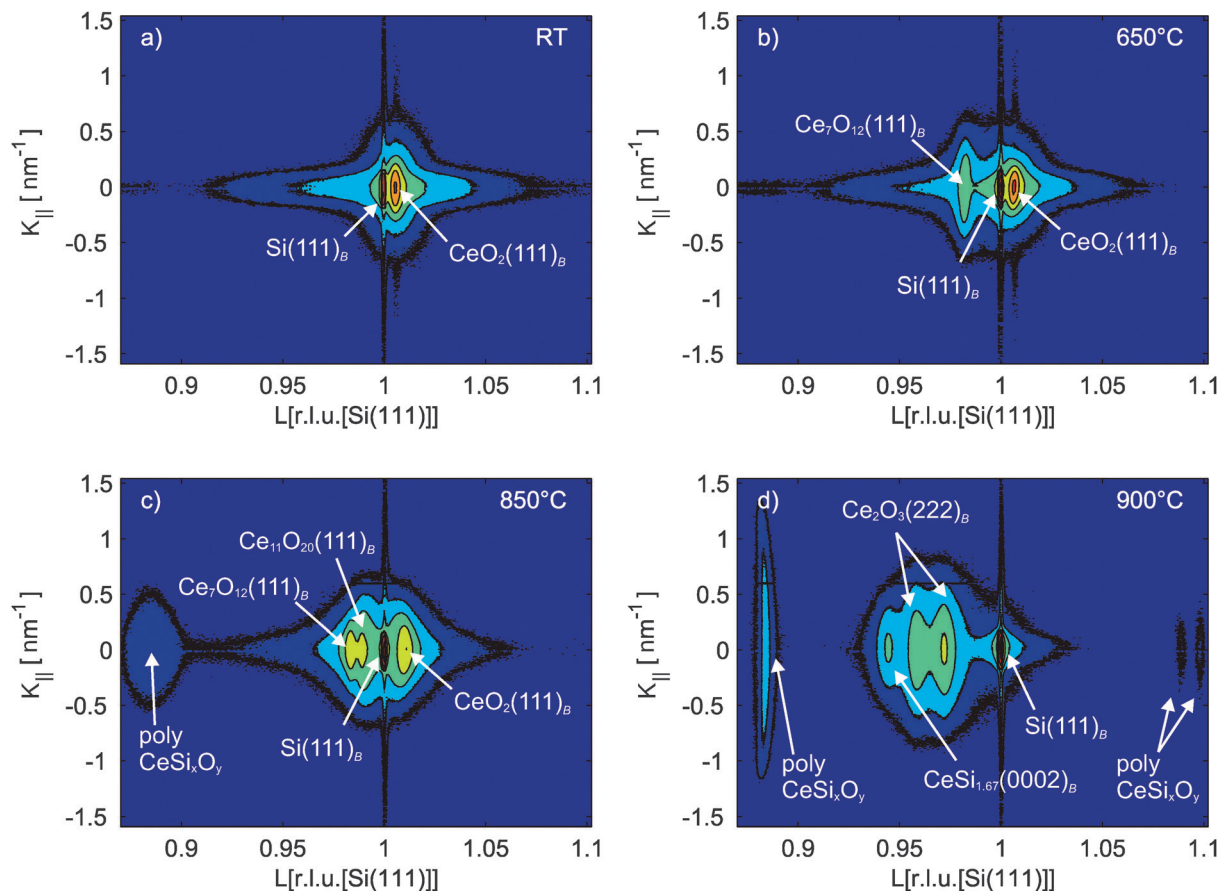


Fig. 8 Reciprocal space mappings close to the Si(111) Bragg peak obtained for annealing at different temperatures. The measurements are performed at RT. After annealing above 850 °C, elongated features pointing to a polycrystalline structure appear at $L = 0.89, 1.09, 1.10$.

temperature of 650 °C. For treatments at higher temperatures, the fringes are diminished due to a roughening of the buffer layer or a reaction between the ceria film and praseodymia buffer layer.

The Bragg peak corresponding to the praseodymia buffer layer is shifted to lower L values than expected for the hex- $\text{Pr}_2\text{O}_3(0002)_\text{B}$ peak ($L = 1.044$) indicating an oxidation of the buffer layer during ceria growth. In addition, no Bragg peaks attributed to hex- $\text{Pr}_2\text{O}_3(0001)$ at $L = 0.522$ and 1.566 were observed (not shown here). Thus, the praseodymia buffer layer has been transformed to a cubic structure due to the additional oxygen content supplied by the ceria film. An accurate determination of the position of the praseodymia Bragg peak is very difficult due to its weak intensity in comparison with the high intensity of the close Si(111) $_\text{B}$ Bragg peak. An estimation can be made using a simulation within the kinematic diffraction theory. The results of such simulations point to a L value between cub- $\text{Pr}_2\text{O}_3(222)_\text{B}$ ($L = 0.974$) and $\text{Pr}_6\text{O}_{11}(111)_\text{B}$ ($L = 0.997$). Hence, we assume an oxidation of the buffer layer during growth in contrast to the growth of thinner ceria films on a hex- $\text{Pr}_2\text{O}_3(0001)$ buffer layer reported previously.⁸

After applying PDA temperatures of 650 °C and 700 °C, further diffraction peaks appear at $L = 0.982$ and $L = 0.988$, respectively. Since the intermediate phases are based on the

fluorite type CeO_2 lattice with ordered oxygen vacancies, the stoichiometry of CeO_x can be determined using the concept of the pseudo-cubic lattice parameter^{20,50} predicting the linear relationship

$$x = -3.945 \text{ \AA}^{-1} \cdot c + 14.329, \quad (2)$$

between the stoichiometry parameter x and the layer distance c as shown in Fig. 10. Therefore, the peaks of the intermediate phases can be attributed to the $\iota(\text{Ce}_7\text{O}_{12})$ and $\delta(\text{Ce}_{11}\text{O}_{20})$ phases of ceria¹⁹ having the layer spacings of $c_{\text{Ce}_7\text{O}_{12}} = 3.193 \text{ \AA}$ and $c_{\text{Ce}_{11}\text{O}_{20}} = 3.174 \text{ \AA}$, respectively. The larger layer distances of the reduced phases result from the $\text{Ce}^{4+} \rightarrow \text{Ce}^{3+}$ transition yielding a larger ion radius. Note that the pseudo-cubic lattice parameters are based on the bulk structures of ceria and do not consider any strain effects which may appear in thin films. For the film studied here, the intensity of the $\text{Ce}_7\text{O}_{12}(111)_\text{B}$ and $\text{Ce}_{11}\text{O}_{20}(111)_\text{B}$ peaks increases with increasing PDA temperature.

Furthermore, the $\text{Ce}_7\text{O}_{12}(111)_\text{B}$ and $\text{Ce}_{11}\text{O}_{20}(111)_\text{B}$ peaks disappear when the XRD measurements are carried out at elevated temperatures and reappear after the sample is cooled (results not shown) while the $\text{CeO}_2(111)_\text{B}$ peak does not vanish at these temperatures. A possible explanation for this temperature related behavior is a high Debye–Waller factor or an order–disorder

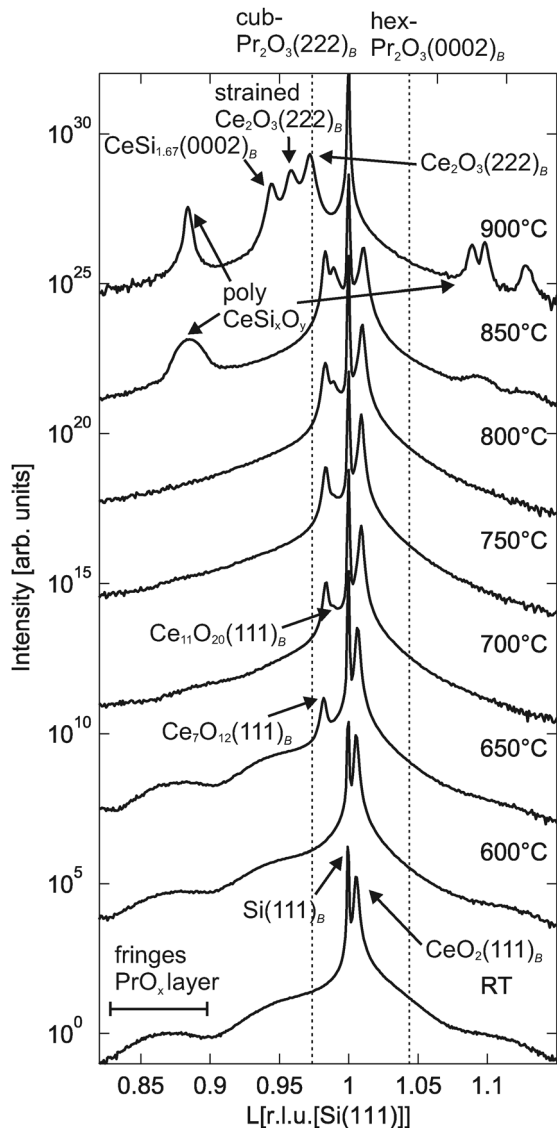


Fig. 9 Specular (00L) XRD scans close to the Si(111)_B Bragg peak of the substrate. The samples are annealed at temperatures up to 900 °C for 30 min. After each temperature step, the samples are cooled to RT and the measurements are performed. The as grown sample shows only the CeO₂(111) peak next to the substrate. At temperatures above 600 °C and 650 °C peaks attributed to Ce₇O₁₂(111) and Ce₁₁O₂₀(111) appear, respectively. Thereafter, silicide and silicate peaks appear at temperatures above 800 °C. The observed fringes correspond to the underlying praseodymia buffer layer. The Bragg peak of the buffer layer seems shifted to L values close to the cub-Pr₂O₃(222)_B peak rather than that expected for the hex-Pr₂O₃(0002)_B peak (dashed lines). Therefore, an oxidation of the praseodymia layer during growth is assumed.

transition due to the high mobility of lattice oxygen at high temperatures. The latter effect leads also to a disordered arrangement of oxygen vacancies and subsequent loss of the superstructure. On the other hand, the CeO₂(111)_B peak shifts to lower L values (corresponding to higher layer distances) as expected due to thermal expansion when measured at elevated temperatures.

The reason for the smaller layer distance of the CeO₂ film in comparison to the bulk structure (*cf.* Fig. 11(a)) for low PDA

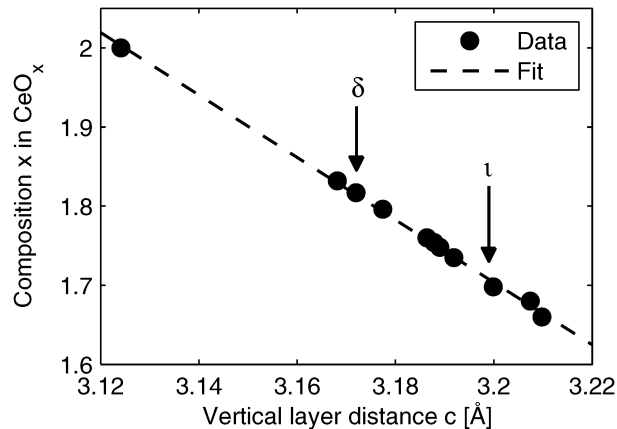


Fig. 10 Composition of the film expressed as the stoichiometry parameters x plotted against the vertical layer distance c according to the pseudo-cubic lattice parameters given by ref. 20 and 50.

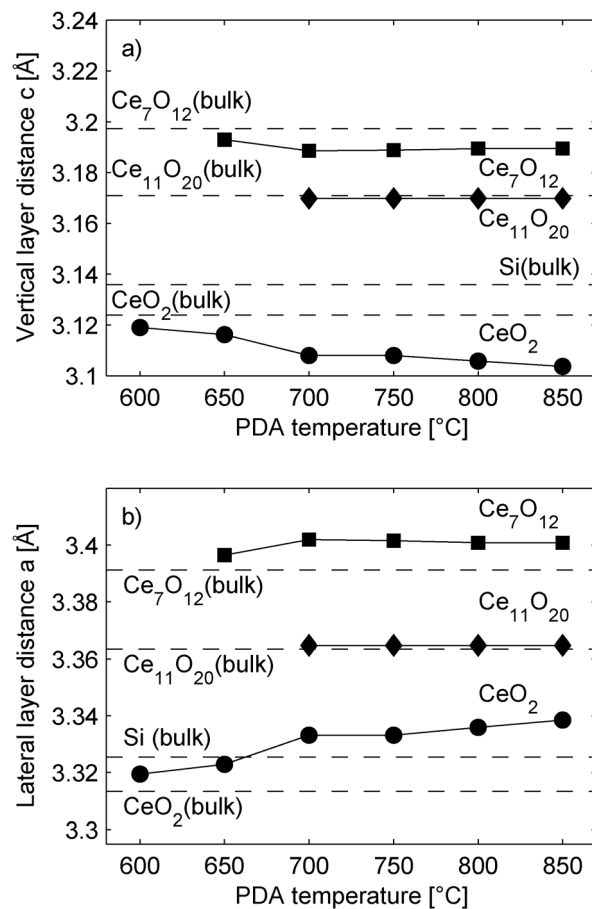


Fig. 11 (a) Vertical layer distance of the appearing ceria phases plotted against the PDA temperature. The stoichiometry of the different phases was determined by using their pseudo-cubic lattice constants from eqn (2). (b) Lateral layer distance determined from eqn (3). The layer distances of the CeO₂ and Ce₇O₁₂ differ from the bulk value indicating strained films while the Ce₁₁O₂₀ phase is fully relaxed.

temperatures is tensile lateral strain based on the lattice mismatch between the CeO₂(111) film and the praseodymia

buffer layer.⁸ With increasing PDA temperature the CeO₂(111)_B peak shifts to larger L values (smaller layer distances) while the Ce₇O₁₂(111)_B and Ce₁₁O₂₀(111)_B peak positions do not change significantly (*cf.* Fig. 9 and 11(a)). Assuming a tetragonally distorted film with biaxial in-plane strain Δa , the lateral layer distance a of the appearing phases can be determined using the relation

$$\frac{\Delta a}{a_{\text{bulk}}} = -\frac{1-\nu}{2\nu} \frac{\Delta c}{c_{\text{bulk}}} \quad (3)$$

as derived by Hashimoto *et al.*,⁵¹ where $\nu \approx 0.3$ is the Poisson ratio of CeO₂.⁵² The CeO₂ Poisson ratio is used for the calculations of all appearing phases since values of the Poisson ratio for the intermediate phases are not available in literature. The occurring error can be neglected since the structures of the intermediate phase are dominated by the cation sublattice which does not change significantly during reduction. The results for the lateral layer distance of the three phases are presented in Fig. 11(b). With increasing PDA temperature, the calculated lateral layer distance of CeO₂ shifts to higher values. Hence, the tensile strain of the remaining CeO₂(111) film is increased with higher temperatures. PDA treatments above 700 °C do not change the lateral layer distances of the Ce₇O₁₂ and Ce₁₁O₂₀ phase. In comparison with the bulk values, the Ce₇O₁₂ exhibits strain similar to the CeO₂ phase while the Ce₁₁O₂₀ phase is fully relaxed.

After a PDA treatment at 900 °C, the three oxide peaks described above vanish and are replaced by peaks at $L = 0.972$, $L = 0.959$ and $L = 0.944$ (*cf.* Fig. 9). The peak at $L = 0.972$ corresponds to a vertical layer distance of $c_{\text{Ce}_2\text{O}_3} = 3.226$ Å and can be attributed to the cub-Ce₂O₃(222)_B Bragg peak of the bulk bixbyite phase of Ce₂O₃ (bulk $c_{\text{cub-Ce}_2\text{O}_3} = 3.222$ Å). Thus, the different oxide phases are transformed into the ceria phase of lowest oxygen content. In addition, no Bragg peaks of the hexagonal Ce₂O₃ phase ($L = 0.518, 1.036, 1.554, \text{etc.}$) are observed. Thus, the cubic phase of Ce₂O₃ is formed exclusively.

The peak at $L = 0.959$ corresponds to a layer distance of $c_{\text{Ce}_2\text{O}_3(s)} = 3.270$ Å and can be attributed to a strained cub-Ce₂O₃ film.¹⁰ In comparison with the bulk value of Ce₂O₃, this vertical layer distance is 1.36% larger indicating a compressive lateral strain based on the lateral lattice mismatch of cub-Ce₂O₃(111) with respect to Si(111) (+2.70%).

Furthermore, the peak at $L = 0.944$ can not be assigned to any ceria phase and exhibits a larger periodicity ($L = 0.472, 0.944, 1.416, \text{etc.}$), resulting in a layer distance of $c = 6.642$ Å. Taking into account the surface sensitive LEED and XPS measurements, we attribute this peak to the hex-CeSi_{1.67}(0002)_B Bragg peak of the hexagonal CeSi_{1.67} phase proposed by Manke *et al.*⁴²

4 Discussion

The SPA-LEED and XRD measurements reveal that the structure of the grown CeO₂(111) film and the praseodymia buffer layer is stable up to PDA temperatures of 650 °C. In contrast to these results the XPS data show a slight reduction of the near surface

region indicating the formation of disordered oxygen vacancies in the low temperature region. At higher temperatures SPA-LEED and XPS measurements show a continuous reduction of the near surface region while the bulk sensitive XRD measurements reveal that the entire film is not reduced since the CeO₂(111)_B Bragg peak is detected up to PDA temperatures of 850 °C. In addition, a second intermediate phase (Ce₁₁O₂₀) is formed at 700 °C which exhibits a higher oxygen content as the earlier formed Ce₇O₁₂ phase. Since an increase of the oxygen content is not detected in the surface studies, we assume that this phase is formed either at the interface between the Ce₇O₁₂ and the CeO₂ crystallites or at the interface region close to the silicon substrate. In the latter case, similar to the growth of the CeO₂(111) films,⁸ oxygen has to be transported into the substrate resulting in the formation of amorphous SiO₂ at the interface between film and the substrate. We assume that a lower diffusion rate of oxygen into the substrate in comparison to the oxygen desorption at the surface is responsible for the formation of the Ce₁₁O₂₀ phase at the interface between film and the substrate. This assumption is supported by the vanishing of the fringes due to the praseodymia buffer layer in the XRD measurements (*cf.* Fig. 9). This indicates an interface reaction, *e.g.* roughening of the praseodymia interface or an intermixing of the praseodymia and ceria films at temperatures above 650 °C. In addition, the tensile strain of the CeO₂ film increases with higher annealing temperatures. Possible reasons for the increasing strain are the lateral lattice mismatch between Ce₁₁O₂₀(111) and CeO₂(111) or the strong thermal expansion of the CeO₂(111) at elevated temperatures. Thus, more research has to be done to elucidate the role of the interface.

Comparing the diffraction measurements with the XPS results, a temperature offset for the formation of the ι -phase (Ce₇O₁₂) is observed. This phase is formed at 660 °C if the sample is heated *via* resistive heating as done for the XRD and SPA-LEED experiments. On the contrary, the ι -phase confirmed using a conventional LEED setup is formed in the XPS experiments at ≈ 800 °C when annealed *via* filament heating. We can exclude an experimental error in temperature control since the Ce₂O₃ phase with the lowest oxygen content and the silicide are formed at the same temperatures in both experimental setups. Thus, a possible explanation for the offset are the different cooling rates based on the experimental setup. Hence, we assume that for an annealing time of 30 min used in our experiments, the samples were not in the thermodynamical equilibrium. For the lower cooling rates (XPS experiments), oxygen from deeper layers of the oxide film diffuses to the surface since the oxide film is exposed to higher temperatures for longer times compared to the diffraction experiments. Hence, the superstructure formed at high annealing temperatures is modified during the cooling process due to re-oxidation. We conclude that the cooling rate has a strong impact on the formation of the superstructures.

The XRD measurements show that polycrystalline CeSi_xO_y or CeSi_x phases are formed after annealing at 850 °C which can not be attributed to any known cerium silicate or silicide.

This phase becomes more pronounced at 900 °C and is also detected at the surface *via* SPA-LEED. In addition, a single crystalline cerium silicide (CeSi_{1.67}) is detected in the SPA-LEED and XRD studies.

The results from the XRD and SPA-LEED measurements clearly reveal that the appearing Ce₂O₃ phase has a bixbyite structure (cub-Ce₂O₃). This is in contrast to studies of bulk single crystals where the hexagonal phase (hex-Ce₂O₃) is the most stable.^{53,54} Hence, the silicon substrate has a stabilization effect on the cub-Ce₂O₃ phase.

Furthermore, SPA-LEED measurements show a ($\sqrt{27} \times \sqrt{27}$)R30° superstructure appearing in a very narrow region of PDA temperatures close to the temperature for the transition to cub-Ce₂O₃. Different to the *t* phase, this diffraction pattern can not be attributed to the surface termination of any well known bulk phase of ceria stable at room temperature and thus, we assume a film with stoichiometry close to Ce₂O₃ is stabilized at the near surface region.

Moreover, it should be mentioned that the color of the sample changes from purple (RT) to cyan (890 °C) during the PDA treatment. Above a PDA temperature of 900 °C the sample turns mat gray due to the silicide formation (see also ref. 48). After a few minutes at a temperature of 930 °C parts of the sample have metallic luster while the current needed for the resistive heating increases drastically.

5 Conclusion

In this study the influence of PDA on the structure and surface stoichiometry was investigated for a thin ceria film (250 nm) grown on a hex-Pr₂O₃(0001)–Si(111) system. It was shown that several crystalline phases with long range ordered oxygen vacancies can be stabilized which may be used for magnetic and catalytic applications in the future. Furthermore, it was revealed that the bulk and surface exhibit a different behavior during reduction. The XRD measurements reveal that higher oxidized phases are still present in the bulk of the film while the oxygen content at the surface is continuously reduced as shown by XPS and SPA-LEED. In addition, it is clearly shown that fully reduced ceria films (Ce₂O₃) exhibit bixbyite structure if grown on Si(111). PDA treatments at very high temperatures lead to the formation of polycrystalline silicate and crystalline silicide.

Acknowledgements

The authors gratefully acknowledge support by the Deutsche Forschungsgemeinschaft (DFG) *via* grant no. WO533/16-1, RE 1186/12-1, BA 1710/17-1 and SCHR1123/4-1 and by the COST Action CM1104. We like to thank W. Caliebe for beamline support during synchrotron experiments carried out at HASYLAB/DESY.

References

- 1 A. Trovarelli, *Catal. Rev. Sci. Eng.*, 1996, **38**, 439.
- 2 A. F. Diwell, R. R. Rajaram, H. A. Shaw and T. J. Treux, The role of ceria in three-way catalysts, in *Catalysis Automotive*

- Pollution Control*, ed. A. Cruq, Elsevier, Amsterdam, 1991, vol. 71.
- 3 G. A. Deluga, J. R. Salge, L. D. Schmidt and X. E. Verykios, *Science*, 2004, **303**, 993.
- 4 S. Torbrügge, M. Reichling, A. Ishiyama, S. Morita and O. Custance, *Phys. Rev. Lett.*, 2007, **99**, 056101.
- 5 T. Campbell, *Surf. Sci. Rep.*, 1997, **27**, 1.
- 6 R. Henry, *Surf. Sci. Rep.*, 1998, **31**, 231.
- 7 M. Bäumer and H.-J. Freund, *Prog. Surf. Sci.*, 1999, **61**, 127.
- 8 M. H. Zoellner, J. Dabrowski, P. Zaumseil, A. Giussani, M. A. Schubert, G. Lupina, H. Wilkens, J. Wollschläger, M. Reichling, M. Bäumer and T. Schroeder, *Phys. Rev. B: Condens. Matter Mater. Phys.*, 2012, **85**, 035302.
- 9 H. H. Pieper, C. Derks, M. H. Zoellner, R. Olbrich, L. Tröger, T. Schroeder, M. Neumann and M. Reichling, *Phys. Chem. Chem. Phys.*, 2012, **14**, 15361.
- 10 J. I. Flege, B. Kaemena, S. Gevers, F. Bertram, T. Wilkens, D. Bruns, J. Bätjer, T. Schmidt, J. Wollschläger and J. Falta, *Phys. Rev. B: Condens. Matter Mater. Phys.*, 2011, **84**, 235418.
- 11 T. Inoue, Y. Yamamoto, S. Koyama, S. Suzuki and Y. Ueda, *Appl. Phys. Lett.*, 1990, **56**, 1332.
- 12 J. Zarraga-Colina, R. M. Nix and H. Weiss, *Surf. Sci.*, 2004, **563**, L251.
- 13 R. K. Singhal, P. Kumari, A. Samariya, S. Kumar, S. C. Sharma, Y. T. Xing and E. Saitovitch, *Appl. Phys. Lett.*, 2010, **97**, 172503.
- 14 R. K. Singhal, P. Kumari, S. Kumar, S. N. Dolia, Y. T. Xing, M. Alzamora, U. P. Deshpande, T. Shripathi and E. Saitovitch, *J. Phys. D: Appl. Phys.*, 2011, **44**, 165002.
- 15 M. Chandra Dimri, H. Khanduri, H. Kooskora, J. Subbi, I. Heinmaa, A. Mere, J. Krustok and R. Stern, *Phys. Status Solidi A*, 2012, **209**, 353.
- 16 V. Fernandes, R. J. O. Mossaneck, P. Schio, J. J. Klein, A. J. A. de Oliveira, W. A. Ortiz, N. Mattoso, J. Varalda, W. H. Schreiner, M. Abbate and D. H. Mosca, *Phys. Rev. B: Condens. Matter Mater. Phys.*, 2009, **80**, 035202.
- 17 Y. Q. Song, H. W. Zhang, Q. Y. Wen, H. Zhu and J. Q. Xiao, *J. Appl. Phys.*, 2007, **102**, 043912.
- 18 X. Han, J. Lee and H. I. Yoo, *Phys. Rev. B: Condens. Matter Mater. Phys.*, 2009, **79**, 100403.
- 19 P. R. Subramanian, Ce-O (cerium-oxygen), in *Binary Alloy Phase Diagrams*, ed. T. B. Massalski, ASM International, Materials Park, 2nd edn, 1990, vol. 2, pp. 1089–1091.
- 20 E. A. Kümmerle and G. Heger, *J. Solid State Chem.*, 1999, **147**, 485.
- 21 D. J. M. Bevan, *J. Inorg. Nucl. Chem.*, 1955, **1**, 49.
- 22 H. Wilkens, O. Schuckmann, R. Oelke, S. Gevers, A. Schaefer, M. Bäumer, M. H. Zoellner, T. Schroeder and J. Wollschläger, *Appl. Phys. Lett.*, 2013, **102**, 111602.
- 23 A. Schaefer, T. Schroeder, G. Lupina, Y. Borchert, J. Dabrowski, C. Wenger and M. Bäumer, *Surf. Sci.*, 2007, **601**, 1473.
- 24 T. Schroeder, T.-L. Lee, L. Libralesso, I. Joumard, J. Zegenhagen, P. Zaumseil, C. Wenger, G. Lupina, G. Lippert, J. Dabrowski and H.-J. Müssig, *J. Appl. Phys.*, 2005, **97**, 074906.

- 25 F. Bertram, C. Deiter, K. Pflaum and O. H. Seeck, *Rev. Sci. Instrum.*, 2012, **83**, 083904.
- 26 A. Schaefer, S. Gevers, V. Zielasek, T. Schroeder, J. Falta, J. Wollschläger and M. Bäumer, *J. Chem. Phys.*, 2011, **134**, 054701.
- 27 J. P. Holgado, G. Munuera, J. P. Espinós and A. R. González-Elipe, *Appl. Surf. Sci.*, 2000, **158**, 164.
- 28 D. R. Mullins, S. H. Overbury and D. R. Huntley, *Surf. Sci.*, 1998, **409**, 307.
- 29 W. Xiao, Q. Guo and E. G. Wang, *Chem. Phys. Lett.*, 2003, **368**, 527.
- 30 E. Paparazzo, G. M. Ingo and N. Zacchetti, *J. Vac. Sci. Technol., A*, 1991, **9**, 1416.
- 31 M. L. Trudeau, A. Tschope and J. Y. Ying, *Surf. Interface Anal.*, 1995, **23**, 219.
- 32 J. P. Holgado, R. Alvarez and G. Munuera, *Appl. Surf. Sci.*, 2000, **161**, 301.
- 33 A. Allahgholi, J. I. Flege, S. Thiess, W. Drube and J. Falta, 2013, in preparation.
- 34 E. J. Preisler, O. J. Marsh, R. A. Beach and T. C. McGill, *J. Vac. Sci. Technol., B*, 2001, **19**, 1611.
- 35 A. Kotani and H. Ogasawara, *J. Electron Spectrosc. Relat. Phenom.*, 1992, **60**, 257.
- 36 J. C. Fuggle, F. U. Hillebrecht, Z. Zolnierrek, R. Lässer, Ch. Freiburg, O. Gunnarsson and K. Schönhammer, *Phys. Rev. B: Condens. Matter Mater. Phys.*, 1983, **27**, 7330.
- 37 E. Wuilloud, H. R. Moser, W.-D. Schneider and Y. Baer, *Phys. Rev. B: Condens. Matter Mater. Phys.*, 1983, **28**, 7354.
- 38 G. Praline, B. E. Koel, R. L. Hance, H.-I. Lee and J. M. White, *J. Electron Spectrosc. Relat. Phenom.*, 1980, **21**, 17.
- 39 A. Laachir, V. Perrichon, A. Badri, J. Lamotte, E. Catherine, J. C. Lavalley, J. El Fallah, L. Hilaire, F. Le Normand, E. Quéméré, G. N. Sauvion and O. Touret, *J. Chem. Soc., Faraday Trans.*, 1991, **97**, 1601.
- 40 S. Gevers, T. Weisemoeller, B. Zimmermann, F. Bertram, C. Deiter and J. Wollschläger, *J. Phys.: Condens. Matter*, 2009, **21**, 175408.
- 41 S. Gevers, T. Weisemoeller, B. Zimmermann, C. Deiter and J. Wollschläger, *Phys. Status Solidi C*, 2010, **7**, 292.
- 42 I. Manke, H. J. Wen, A. Bauer, M. Dähne-Prietsch and G. Kaindl, *J. Vac. Sci. Technol., B*, 1995, **13**, 1657.
- 43 A. Fujimori, M. Grioni, J. J. Joyce and J. H. Weaver, *Phys. Rev. B: Condens. Matter Mater. Phys.*, 1987, **36**, 1075.
- 44 M. Henzler, *Appl. Phys. A: Mater. Sci. Process.*, 1984, **34**, 205.
- 45 M. Henzler, *Surf. Rev. Lett.*, 1997, **4**, 489.
- 46 T.-M. Lu and M. G. Lagally, *Surf. Sci.*, 1982, **120**, 47.
- 47 J. Wollschläger, *Surf. Sci.*, 1995, **328**, 3.
- 48 R. Olbrich, H. H. Pieper, R. Oelke, H. Wilkens, J. Wollschläger, M. H. Zoellner, T. Schroeder and M. Reichling, *Phys. Chem. Chem. Phys.*, 2013, submitted.
- 49 S. Torbrügge, M. Cranney and M. Reichling, *Appl. Phys. Lett.*, 2008, **93**, 073112.
- 50 S. P. Ray, A. S. Nowick and D. E. Cox, *J. Solid State Chem.*, 1975, **15**, 344.
- 51 S. Hashimoto, J. L. Peng, W. M. Gibson, L. J. Schowalter and R. W. Fathauer, *Appl. Phys. Lett.*, 1985, **47**, 1071.
- 52 V. Kanchana, G. Vaitheeswaran, A. Svane and A. Delin, *J. Phys.: Condens. Matter*, 2006, **18**, 9615.
- 53 J. L. F. Da Silva, *Phys. Rev. B: Condens. Matter Mater. Phys.*, 2007, **76**, 193108.
- 54 H. Bärnighausen and G. Schiller, *J. Less-Common Met.*, 1985, **110**, 385.